Coherence loss in light backscattering by random media with nanoscale nonuniformities

Anatol M. Brodsky, Gordon T. Mitchell, Summer L. Ziegler,* and Lloyd W. Burgess
Center for Process Analytical Chemistry, Department of Chemistry, University of Washington, Seattle, Washington 98195-1700, USA
(Received 1 December 2006; published 13 April 2007)

An experimental technique for measuring time-resolved coherence loss and destruction of backscattered wave packets in random media is described. The results of such measurements, performed with a modified Michelson interferometer, contain rich information about the characteristics of media nonuniformities. Experimental data for model nanosuspensions are compared with theoretical expressions developed in the paper which include the effects of Mie-type resonant scattering. We attribute one such observed effect to enhanced ineleastic optical transitions near the surface of nonmetallic nanoparticles. The inverse problem of characterization of multiscattering random media by backscattering is also considered.

DOI: 10.1103/PhysRevE.75.046605 PACS number(s): 42.25.−p, 42.30.−d, 42.90.+m, 87.64.Cc

I. INTRODUCTION

Coherence effects in the propagation of optical and other classical and quantum waves in multiscattering nonuniform media have attracted a great deal of attention during the last 25 years. Because both constructive and destructive interference of multiply scattered waves can occur in such media, a variety of peculiar effects including fluctuational waveguiding and wave localization can occur. The consequences of such effects in random systems are qualitatively different from those occurring in the optics of regular crystal-type structures and thus require new theoretical approaches to accurately describe them.

The propagation of electromagnetic waves in random structures has traditionally been described using a photon diffusion model. In typical diffusion models, it is assumed that phase information is partly or completely lost after a finite number of scattering events as described by the transport mean free path, ℓ_{mp}, which is the distance electromagnetic waves travel in the medium before their phase characteristics are randomized. However, phase effects can in fact survive in random media after multiple light scattering events at relatively long distances and can lead to nontrivial phenomena not predicted by the framework of diffusion theory. The possibility of the manifestation of such phase-dependent interference effects in multiscattering media was suggested in pioneering works by Watson [1] and De Wolf [2] and remains a subject of great interest. For a broader view of this topic in the literature, see [3–10].

The realization of such an effect in optics was first experimentally confirmed in 1984 by Kuga and Ishimaru and in 1985 by van Albada and Langedijk and by Wolf and Maret [10]. In these experiments, the characteristics of the backscattered light were measured using incoherent intensity detection methods. Our study of the coherence loss in backscattered light can be considered as a further advancement of the above-mentioned works using coherent signal detection.

In this work, the detailed coherence structure of light backscattered from a bulk system with nanoscale nonuniformities was investigated. Aqueous suspensions of noninteracting mesoscopic spherical particles were used as a simple experimental model. The measurements, collected with the help of a modified Michelson interferometer, allow us to compare two parts of a split incident wave packet; a reference wave packet and a signal wave packet which has been reflected and partially destroyed after traveling in the bulk sample as the result of scattering by large scale and short scale nonuniformities. These measurements can be considered as the optical realization of the type of experiments proposed in nuclear physics and mentioned by Dodd and McCarthy [11] as early as 1964. By changing the optical length of the travel distance for the reference wave packet before mixing both packets, it is possible to examine the characteristics of light coherently reflected from the nonuniform sample bulk after different dwell distances, ℓ, inside the sample. Such examinations open new possibilities for detailed *in situ* optical evaluation of the statistical and dynamic characteristics of multiscattering systems of nanoparticles and other mesoscopic irregular structures with dimensions from a few to hundreds of nanometers.

Possible applications of this technique include analysis of particle suspensions, colloidal dispersions, and polymer solutions. Such evaluations are important in a number of new nanotechnologies [12,13] and medical diagnostics and therapies [14]. To realize this potential, however, it is necessary to solve the nontrivial inverse problem; that is, to find theoretical expressions for the relation between observed signals and studied system properties. In this paper, we construct such a theoretical model following the general ideas proposed in our previous work [15].

The first theoretical problem is to relate light propagation characteristics with individual scatterer properties in a medium containing randomly distributed scatterers. This difficult problem, known as the radiative transfer problem, lacks an exact analytical solution in the case of electromagnetic waves in three-dimensional multiscattering media [5,16]. Our approach, analogous in some aspects to the introduction of the Fermi pseudopotential in neutron scattering [17], is based on an approximate expression for the effective dielectric function of the system [18] which is valid for the case of large numbers of randomly distributed particles. An important characteristic of this approximation is that it expresses dielectric functions through the sum of individual scattering

*Present address: Pacific Northwest National Laboratory, P.O. Box 999, Richland, WA 99352, USA

amplitudes while taking into account interference effects.

The other central feature of our theory is the application of Fock's method for the expression of a formal solution of wave equations in exponential form with the help of the introduction of an additional coordinate. Such expressions allow us to perform a quasi-Gaussian averaging over the particle distribution based on functional integral techniques [19,20]. In our calculations we have also taken into account the vector nature of light. Although substantially simpler scalar-wave models have been useful in some instances, it is becoming increasingly apparent that they fail to correctly describe many important characteristics of optical phenomena in random media.

To compare our theoretical model and the experimental results, it is necessary to have expressions for the scattering amplitudes of individual particles. Especially interesting and important for practical applications is the resonance frequency interval, where the wavelength of light is comparable to the particle perimeter. In this work, approximate expressions based on the Mie solution [18,21] for the amplitudes of scattering by individual uniform spherical particles are used. One of the important properties of such amplitudes is an appearance of resonances described in Mie's works over 100 years ago. Analogous resonances, which can be considered as the specific realization of so-called Redge poles when analyzed in general wave scattering theory [18], also have to be present, albeit with specific structures, during scattering by nanoparticles of different shapes and structures. They have been observed in the cross section of light scattered by individual particles. The results described in this paper provide the experimental confirmation that resonances of the Mie type can be clearly identified in the scattering by randomly distributed systems of particles, as it was supposed in our earlier paper [15] and by Kim and Ishimaru [16]. The drastic increase of the electromagnetic field near nonmetallic nanoparticles in the parameter intervals corresponding to Mie resonances, where particles function as individual resonant antennas, opens the possibility of observing and exploiting different surface-enchanced noneleastic optical transitions. We discuss this possibility further in the conclusion.

The paper is organized as follows: the experimental device, model systems, and main experimental results are described in Sec. II. The theory developed in the framework of the nonperturbative method is provided in Sec. III, with calculation details described in Appendixes A and B. The comparison between experimental results and theory is considered in Sec. IV. In the concluding Sec. V, the general results are summarized and possible future applications and generalizations of the described experimental and theoretical techniques are discussed.

II. EXPERIMENT

The Optiphase, Inc. optical coherence domain interferometer [22] is the main element of the experimental device shown schematically in Fig. 1. The instrument light source is a superluminescent diode (SLD) with a narrow wave-packet bandwidth of approximately 40 nm centered around 1310 nm. A corning SMF28 single mode optical fiber with a

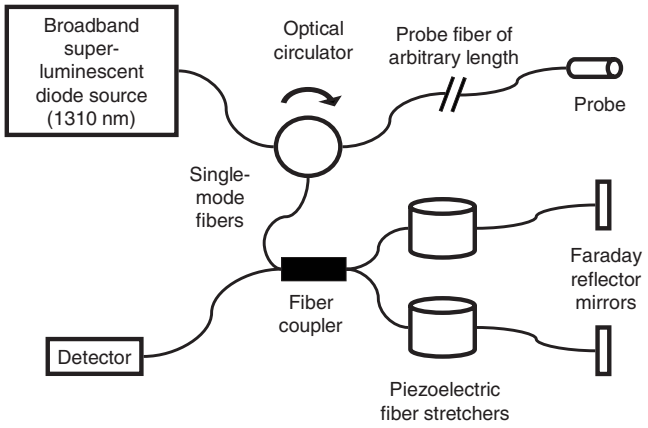

FIG. 1. Block diagram of the Optiphase instrument used in this experiment. The piezoelectric fiber stretchers and Faraday reflector mirrors form the two arms of a Michelson interferometer. Applying a potential to the piezoelectric units stretches the optical fiber wound around them, thus varying the optical distance the wave packets travel. This allows detection of coherently backscattered wave packets as a function of photon dwell distance, ℓ, in the sample matrix.

9 μm core is used throughout the instrument. A circulator routes wave packets from the source to the probe and heterogeneous sample, and then directs the scattered wave packets collected by the probe to an interferometer. A triangular potential is applied to piezoelectric fiber stretchers, stretching 40 m of optical fiber wrapped around each stretcher to achieve varying optical path differences between the interferometer arms on the order of a few millimeters. When the optical path difference between the arms is within the coherence length λ_c of the source (approximately 28 μm) and the wave packets from each arm are in phase, constructive interference occurs. Signal processing of the interferogram results in the discrete peaks, followed by a decay pattern, as shown in Fig. 2. The main variable in the measurements defining the signal value is the wave-packet dwell distance, ℓ, which is indicative of the optical path which backscattered wave packets travel in the sample matrix.

The two model systems were composed of suspensions of polymer particles at 0.01 and 0.10 volume fractions purchased from Duke Scientific Corporation [23]. The standards at 0.01 volume fraction were monodisperse polystyrene spheres in an aqueous solution with diameters ranging from 21 nm to 1.745 μm. The mean diameters of the nanospheres were measured using transmission electron microscopy (TEM) and a NIST-traceable calibration, and are provided in Table I. The deviation of sphericity for each standard is less than 1%. The standards at 0.10 volume fraction were narrowly dispersed latex spheres with particle diameters ranging from 30 nm to 2.0 μm, as shown in Table II. Each suspension contained less than 0.1% of a Duke proprietary preservative and less than 0.2% of a Duke proprietary surfactant to prevent coalescence.

Prior to measurement, each standard suspension was inverted three times, sonicated for 30 s, and inverted three additional times. After discarding several drops to waste, approximately 0.5 mL of each sample was placed in a stirred

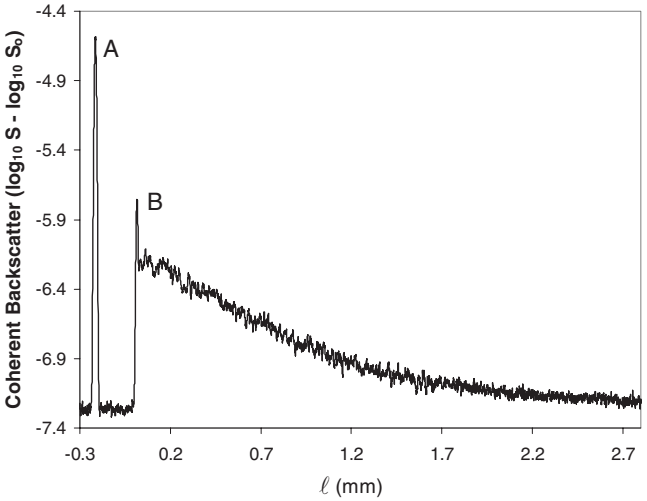

FIG. 2. Signal profile obtained from a 0.01 volume fraction aqueous suspension of 298 nm diameter polystyrene particles. The initial peak, labeled (A), corresponds to Fresnel reflection from the inside of the probe window, while peak (B) is the reflection from the outside of the probe window. Only photons that are coherently backscattered from the polystyrene particles and return to the interferometer are detected. In the case of highly scattering systems, this results in a tailing signal decay immediately following the reflection off the outside of the probe window.

vial for triplicate measurements following a random block experimental design. The probe was inserted directly into the suspensions to ensure measurement of the bulk of the media. The probe is composed of an optical fiber sheathed in a 0.25 in. diameter stainless steel tube slightly offset from a thin glass window set at an 8° angle to minimize the Fresnel reflection from the probe-medium interface. Nevertheless, sharp peaks from both the inside and the outside of the probe window appear before the tailing decay profile generated when the probe is immersed in highly scattering matrices. The peaks from the inside and the outside of the probe window are labeled, respectively, as peaks A and B in Fig. 2.

Due to the probe design utilized in this work, a ratio between the above-mentioned probe window peaks can be used to determine the refractive index difference between the inner window-air and outer window-sample interfaces. Analysis of a series of solvents with refractive indices ranging from 1.3270 to 1.4502 was performed to establish a calibration curve of the relationship between the peak ratios resulting from the probe design and the effective mean refractive index of the sample, as shown in Fig. 3. This calibration was then applied to the suspension systems to determine the effective mean refractive index of the particle suspensions, which was used to find $\tilde{\ell}$, the relative photon dwell distance in the sample matrix.

The decay portions of the signal profiles obtained from the 1% and 10% series of suspensions are shown in Figs. 4 and 5, respectively. These decay profiles are the basis for our comparison of theory and experiment and will be more fully discussed in Sec. IV.

III. THEORY

In the considered experiments, we measured characteristics of light backscattered into the half space $x_1<0$ (medium 1) from an aqueous suspension of particles in the half space $x_1>0$ (medium 2). In the general theoretical description of such experiments, we consider the simplest case of a nonmagnetic system described by the scalar local refractive index

$$n(\omega;\mathbf{x}) = n^*(-\omega;\mathbf{x}) = n_1(\omega)\theta(-x_1) + n_2(\omega;\mathbf{x})\theta(x_1), \quad (1)$$

where ω is the light frequency, $\mathbf{x}$ is the coordinate vector, and $\theta(x_1)$ is the step function. For the sake of simplicity in presentation, the dielectric fluctuations outside the sample (at $x_1<0$) and the differences between the properties of sample bulk and its surface layer are neglected. The sample is assumed to be statistically uniform and the local refractive index $n_2(\omega;\mathbf{x})$ is taken in the following form:

$$n_2(\omega;\mathbf{x}) = n_2^*(-\omega;\mathbf{x}) = \bar{n}_2(\omega) + \kappa(\omega)\frac{\delta N(\mathbf{x})}{\bar{N}},$$

$$\bar{n}_2(\omega) = \langle n_2(\omega;\mathbf{x})\rangle = n_m(\omega) + \kappa(\omega),$$

$$\bar{N} = \langle N(\mathbf{x})\rangle = \sum_\beta \langle N_\beta(\mathbf{x})\rangle, \quad (2)$$

where $n_m(\omega)$ is the refractive index of media surrounding the particle. The angular brackets denote averaging over the studied sample volume and the sum is taken over all types of

TABLE I. Size characteristics of the Duke Scientific 3000-series aqueous polystyrene particle suspensions used in this work. Sample concentration was 0.01 solids by volume.

Particle diameter (nm)	Relative standard deviation of particle diameter (%)
21	7.1
41	4.4
60	4.2
81	3.3
102	2.9
199	3.0
269	2.6
350	2.0
404	1.0
453	0.9
491	0.8
519	1.0
596	1.0
701	0.9
799	1.1
895	0.9
1101	2.1
1361	1.8
1588	1.6
1745	1.4

TABLE II. Size characteristics of the Duke Scientific 5000-series aqueous latex particle suspensions used in this work. Sample concentration was 0.10 solids by volume. The particle size distribution is much broader for the 0.01 volume fraction polystyrene samples of comparable particle dimensions.

Particle diameter (nm)	Relative standard deviation of particlediameter(%)
30	⩽18
60	⩽18
80	⩽18
90	⩽15
100	⩽15
160	⩽6
300	⩽3
340	⩽3
360	⩽3
430	⩽3
600	⩽3
670	⩽3
740	⩽3
870	⩽3
1000	⩽3
1300	⩽5
2000	⩽4

particles β. The function $\delta N(\mathbf{x})$ denotes the local deviation from the mean value of sample characteristics $\bar{N}$ averaged over distances larger than particle radii but less than the wavelength of incident light. In the following, we will suppose that $\delta N(\mathbf{x})$ describes the nonuniformity of the particle concentration distribution. The coefficient $\kappa(\omega)$ in Eq. (2) is related in this case to the amplitude of light scattering by the particles. We express $\kappa(\omega)$ through the individual scattering events with the help of the so-called coherent phase approximation, according to which

$$\kappa(\omega) = \kappa^*(-\omega) = 2\pi\left(\frac{c}{\omega n_m}\,\mathrm{Re}\,\bar{n}_2(\omega)\right)^2 \sum_{(\beta)} \bar{N}_\beta A_\beta(0),$$

$$\mathrm{Im}\,\bar{n}_2(\omega) = \mathrm{Im}\,\kappa(\omega), \tag{3}$$

where $\bar{N}_\beta$ is the mean concentration of particles of the type β, $A_\beta(0)$ is the complex amplitude of forward light scattering by such individual particles, and c is the velocity of light. The imaginary component of $A_\beta(0)$ describes the effects of coherence loss in individual scattering events which lead to the exclusion of scattered wave components from the measured intensity of the main course of traveling coherent wave packets with trajectories defined by the distribution of posi-

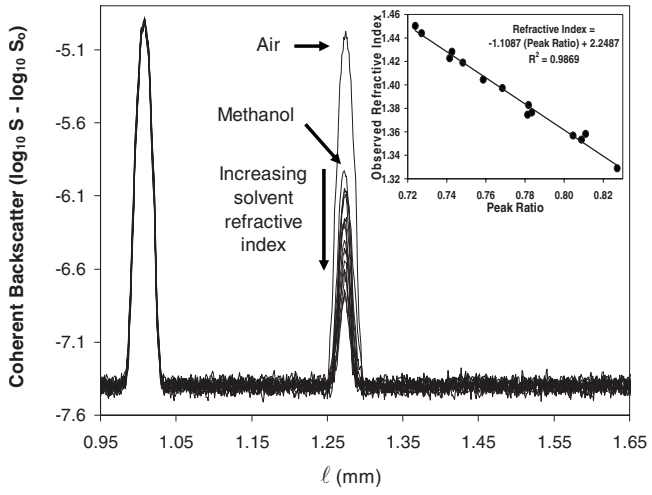

FIG. 3. Detail from decay profiles of a series of solvents. The two sharp peaks result from specular reflection off the inside and outside of the probe window, respectively. The intensity of these peaks depends on the change in effective refractive index which occurs at each window boundary. The inset shows a calibration curve constructed from the ratio of outer to inner window peak intensities, which allows the determination of the effective refractive index of samples placed in contact with the probe.

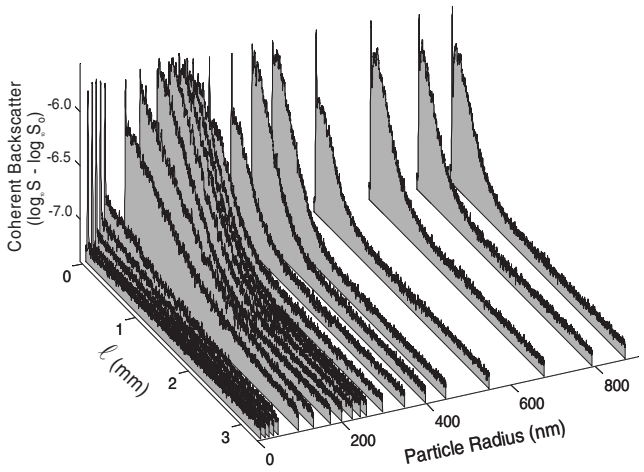

FIG. 4. Decay profiles of a series of 0.01 volume fraction suspensions of polystyrene particles in water. Particle radii range from 10.5 to 872.5 nm. The sharp peak at the beginning of each profile is caused by the reflection off the outside of the probe window.

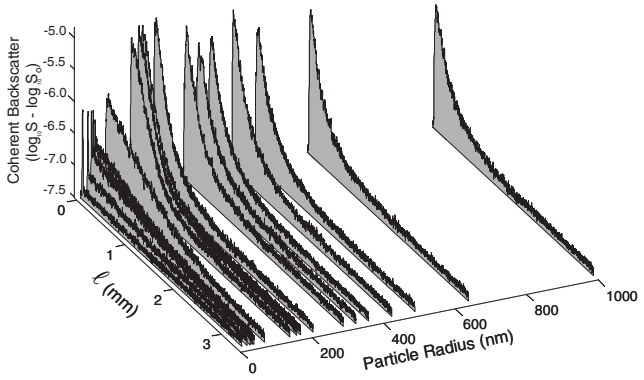

FIG. 5. Decay profiles of a series of 0.10 volume fraction suspensions of latex particles in water. Particle radii range from 15 to 1000 nm.

tions and shapes of nonuniformities averaged over distances larger than wave-packet space widths. For the sake of simplicity, we disregard the effect of direct nonelastic processes in Eq. (3) and correspondingly set $\mathrm{Im}\,\bar{n}_2(\omega)$ equal to $\mathrm{Im}\,\kappa(\omega)$. The generalization which takes into account the possibility of bulk and surface inelastic processes is straightforward. The expression (3) can be valid when

$$|\kappa(\omega)| < \mathrm{Re}\,\bar{n}_2(\omega). \tag{4}$$

The validity condition is less stringent than Eq. (4) in some of the following calculations when only contributions of the imaginary part of $\kappa(\omega)$ are important. The expressions for $A_\beta(0)$ are relatively simple in the following two limits.

(a) In the high wavelength (small particle) limit when it is possible to use the Rayleigh-Gans approximation [18]:

$$\left.\begin{aligned} \mathrm{Re}\,A_\beta(0) &= \left(\frac{\omega}{c}n_m\right)^2 \frac{n_p^2 - n_m^2}{n_p^2 + 2n_m^2} R_\beta^3, \\ \mathrm{Im}\,A_\beta(0) &= \frac{F}{2}\left(\frac{\omega}{c}n_m\right)^3 \left(\frac{n_p^2 - n_m^2}{n_p^2 + 2n_m^2}\right)^2 R_\beta^4 \end{aligned}\right\} \left|\frac{\omega}{c}(n_p - n_m)R\right| < 1, \tag{5}$$

where R_β is the spherically averaged particle dimension, F is a dimensionless form factor of the order of unity, and n_p and n_m are, respectively, the refractive indices of the particle and the surrounding media.

(b) In the short wavelength, Fraunhofer diffraction limit, when

$$\left.\begin{aligned} \mathrm{Re}\,A_\beta(0) &= 0 \\ \mathrm{Im}\,A_\beta(0) &= \frac{\omega}{c}n_m S_\beta \end{aligned}\right\} \quad \text{for } \sqrt{S_\beta} > \frac{c}{\omega}, \quad |n_p - n_m| < n_m, \tag{6}$$

where S_β is the so-called radar cross section of the particle β, which is two times larger than the geometrical cross section [18]. In the case of a spherical particle, S_β does not depend on the direction of light propagation and is equal to $2\pi R_\beta^2$. For the theoretical description, the most nontrivial is the intermediate wave interval between limits (5) and (6) which we call the resonance scattering interval. In this interval, the scattering amplitudes are not monotonic and are critically dependent on shape and other specific particle characteristics. For this reason, the resonance scattering interval provides the most detailed data about multiscattering media characteristics. In this work, where experiments were performed with monodisperse spherical particles for the interpolation between two limits (5) and (6), we use the special approximation for Mie's solution [18,21] for light scattering by uniform dielectric spheres. The approximation is described in Appendix B.

We represent the amplitude of the reference electric field entering in the interferometer coupler, E^{ref}, in the form of the Gaussian wave packet with the center frequency $\omega = \omega_0$ and the bandwidth σ moving along the axis x_1 in the negative direction:

$$E^{\mathrm{ref}} = \frac{E_0^{\mathrm{ref}}}{2\pi\sigma}\int d\omega \exp\left\{-i\left[\omega t + n_1\frac{\omega}{c}(2\ell + x_1)\right] - \frac{(|\omega| - \omega_0)^2}{2\sigma^2}\right\}, \tag{7}$$

where the parameter $n_1\ell$ is a variable optical length traveled by the reference wave packet in the media with refractive index n_1, and E_0^{ref} is its amplitude. The observed signal is proportional to the maximum value of the envelope of the interferogram between E^{ref} and the wave packets with the amplitude $E(\omega;\mathbf{x})$ entering the coupler after backscattering from the sample bulk. This envelope corresponds to signal averaging over a time interval much larger than ω^{-1}. Taking into account such averaging, we take the expression for the value of the signal $T(\ell)$ in the following form:

$$T(\ell) = \mathrm{Max}\langle j(\ell)\rangle,$$

$$j(\ell) = \left\langle \frac{(E_0^{\mathrm{ref}})}{2\pi\sigma}\int d\omega \int_{|\mathbf{x}-\mathbf{x}^0|<L} d^3x \left\{ n_1 E(\omega;\mathbf{x}) \times \exp\left[\frac{i\omega}{c}n_1(2\ell + x_1) - \frac{(|\omega| - \omega_0)^2}{2\sigma^2}\right]\right\}\right\rangle. \tag{8}$$

The angle brackets in Eq. (8) again denote averaging over sample properties, $E(\omega;\mathbf{x})$ is an amplitude of the complex field with frequency ω which is backscattered from the sample with the same polarization as E^{ref} and L is the linear dimension of the interferometer coupler (with the position of its center at $\mathbf{x}^0 = \{x_1^0, 0, 0\}$ with $x_1^0 < 0$). L is supposed to be much larger than both the wavelength and mean distances between nonuniformities in the studied sample. This condition allows us to exclude from the expression for the signal all characteristics of the coupler (such as the structure of its eigenmodes) except its volume $\sim L^3$, as well as effects of diffraction structure from possible small-scale regular arrangements of the sample nonuniformities. The latter effect is averaged in the interferometer signal to zero. In Eq. (8), we have supposed that in the relevant frequency interval $\bar{n}_2(\omega)$ changes with ω relatively slowly and

$$\left|\frac{d\ln n_2(\omega)}{d\ln\omega}\right| < 1 \quad \text{for } \omega_0 - \sigma < \omega < \omega_0 + \sigma. \tag{9}$$

This is not always the case, in particular when the relevant frequencies include an interval of anomalous dispersion.

To obtain an expression for $E(\omega;\mathbf{x})$ convenient for averaging we introduce Debye's potentials $\mathbf{F}^{(1,2)}$ [18]

$$\mathbf{F}^{(1,2)}(\omega,\mathbf{x}) = \mathbf{E}(\omega,\mathbf{x}) \pm \frac{i}{n(\omega;\mathbf{x})}\mathbf{H}(\omega,\mathbf{x}), \tag{10}$$

where $\mathbf{E}(\omega,\mathbf{x})$ and $\mathbf{H}(\omega,\mathbf{x})$ are, respectively, the electric and magnetic vectors. The Maxwell equations for $\mathbf{F}^{(1,2)}$ have the form of the two coupled linear equations:

$$\operatorname{curl}\mathbf{F}^{(1,2)} \mp \frac{\omega}{c}n(\omega;\mathbf{x})\mathbf{F}^{(1,2)} \pm \left[\operatorname{grad}\ln n(\omega;\mathbf{x}), \frac{(\mathbf{F}^{(1)}-\mathbf{F}^{(2)})}{2}\right] = 0, \tag{11}$$

where the square brackets designate the vector product. Note that the modulus of the coefficient grad $\ln n(\omega;\mathbf{x})$ in Eq. (11) is equal to the inverse principal ray curvature at the point $\mathbf{x}$.

In order to perform the calculations in a compact form, we introduce the algebra of operators in a six-dimensional space, which is the direct product $(i\times\alpha)$ of the three-dimensional space $i=1,2,3$ and the two-dimensional photon spin space $\alpha=1,2$ with the following matrix elements of relevant operators I, $I_{k\ell}$, S_k, and $\sigma_{1,3}$:

$$\langle i,\alpha|I|j,\alpha'\rangle = \delta_{ij}\delta_{\alpha,\alpha'},$$

$$\langle i,\alpha|S_k|j,\alpha'\rangle = -(i,\alpha|S_k^*|j,\alpha') = -\delta_{\alpha,\alpha'}ie_{ikj},$$

$$\langle i,\alpha|\sigma_1|j,\alpha'\rangle = \delta_{ij}(\delta_{\alpha1}\delta_{\alpha'2}+\delta_{\alpha2}\delta_{\alpha'1}),$$

$$\langle i,\alpha|\sigma_3|j,\alpha'\rangle = \delta_{ij}(\delta_{\alpha1}\delta_{\alpha'1}-\delta_{\alpha2}\delta_{\alpha'2}), \tag{12}$$

where e_{ijk} is the completely antisymmetric tensor in three-dimensional space with $e_{123}=1$ and δ_{ij} is Kroneker's symbol. Equation (11) can now be rewritten in a matrix form as follows:

$$\sum_{k=1}^{3} i\sigma_3 S_k\frac{\partial}{\partial x_k}F + \frac{\omega}{c}n(\omega;\mathbf{x})F + \frac{I+\sigma_1}{2} \times\sum_{k=1}^{3} i\sigma_3 S_k\frac{\partial\ln n(\omega;\mathbf{x})}{\partial x_k}F = 0, \tag{13}$$

where $F\equiv F(\omega;\mathbf{x})$ is a column:

$$F(\omega;\mathbf{x}) = \begin{vmatrix}\mathbf{F}^{(1)}(\omega;\mathbf{x})\\ \mathbf{F}^{(2)}(\omega;\mathbf{x})\end{vmatrix} \equiv \begin{vmatrix}F_1^{(1)}\\ F_2^{(1)}\\ F_3^{(1)}\\ F_1^{(2)}\\ F_2^{(2)}\\ F_3^{(2)}\end{vmatrix}. \tag{14}$$

The vector $F(\omega,\mathbf{x})$ obeys the following relation:

$$F^*(\omega,\mathbf{x}) = \sigma_1 F(-\omega,\mathbf{x}). \tag{15}$$

We introduce the retarded matrix Green function $G(\omega;\mathbf{x},\mathbf{x}')$, which is the solution of the equation:

$$KG(\omega;\mathbf{x};\mathbf{x}') \equiv \left\{\sum_{k=1}^{3} i\sigma_3 S_k\frac{\partial}{\partial x^k} + \frac{\omega}{c}n(\omega;\mathbf{x}) + \frac{I+\sigma_1}{2}\sum_{k=1}^{3} i\sigma_3 S_k\frac{\partial\ln n(\omega;\mathbf{x})}{\partial x_k}\right\}G(\omega;\mathbf{x},\mathbf{x}') = I\delta^3(\mathbf{x}-\mathbf{x}'). \tag{16}$$

It follows from Eq. (16) and the definition of the retarded Green function that

$$S_1^2\int_{|\mathbf{x}_\parallel-\mathbf{x}_\parallel^0|<L} G(\omega;\mathbf{x};\mathbf{x}')d^2x_\parallel = \frac{1}{2\pi}\exp\left[-i\frac{\omega x_1}{c}n_1(\omega)\right]S_1^2\left[\int_{|\mathbf{x}_\parallel|<L} G(\omega;\mathbf{x},\mathbf{x}')\Big|_{x_1=0} d^2x_\parallel\right] \quad \text{for } x_1\leqslant 0,\ x_1'\geqslant 0;\ \mathbf{x}_\parallel=\{x_2,x_3\}. \tag{17}$$

This result corresponds to the continuity of the tangential components of $\mathbf{E}$ and $\mathbf{H}$ across the sample boundary. With the help of $G(\omega,\mathbf{x},\mathbf{x}')$, we can rewrite expression (8) as follows:

$$T(\ell) = \frac{LI_0}{(2\pi\sigma)^2}\left\langle\left|(F^{(0)})^+\frac{I+\sigma_1}{2}\int_{|\mathbf{x}_\parallel|<L}\delta(x_1)d^3xd^3x'\int d\omega n_1(\omega)\sigma_3\times\left\{\exp\left[-\frac{(|\omega|-\omega_0)^2}{\sigma^2}+i\frac{\omega}{c}\bar{n}_2x_1'-2\frac{i\omega}{c}n_1\ell\right]G(\omega;\mathbf{x},\mathbf{x}')\right.\right.$$
$$\left.\left.\times\left[\frac{\omega}{c}\kappa(\omega)\frac{\delta\rho(\mathbf{x}')}{\bar{\rho}}+\frac{I+\sigma_1}{2}\sum_{k=1}^{3} i\sigma_3S_k\frac{\partial}{\partial x_k'}\ln\left(1+\kappa(\omega)\frac{\delta\rho(\mathbf{x}')}{\bar{\rho}\bar{n}_2}\right)\right]\right\}F^0\right|\right\rangle, \tag{18}$$

where I_0 is the electromagnetic energy flow entering the studied sample bulk and F_0 describes the polarization structure of the incident light. In the following, we suppose that ℓ is larger than $\frac{c}{\sigma}$ and correspondingly it is possible to separate the scattering effects at the sample surface interval with the width smaller than $\frac{c}{\sigma}$. We consider the case of linear polarization when

$$F^{(0)} = \sigma_1 (F^0)^+ = \frac{1}{2} \begin{vmatrix} 0 \\ 1 \\ -i \\ 0 \\ 1 \\ i \end{vmatrix}. \tag{19}$$

Now we introduce, following Fock's idea [19], the fifth, timelike coordinate ν and present the Green function G in the following form:

$$G(\omega;\mathbf{x},\mathbf{x}') = -i\int_0^\infty U(\nu)d\nu \tag{20}$$

where $U(\nu)$ is the matrix function of ν, ω, $\mathbf{x}$, $\mathbf{x}'$ equal to

$$U(\nu) \equiv U(\nu;\omega;\mathbf{x},\mathbf{x}') = e^{iK\nu}\delta^3(\mathbf{x}-\mathbf{x}') \tag{21}$$

with the matrix operator K defined in Eq. (16). In Eq. (20) we have taken into account that

$$\mathrm{Im}\,\frac{\omega}{c} n(\omega;\mathbf{x}) > 0. \tag{22}$$

The matrix $U(\nu)$ has to satisfy the linear differential equation

$$\frac{\partial U}{\partial \nu} = iKU \tag{23}$$

with the boundary condition

$$U(0) = I\delta^3(\mathbf{x}-\mathbf{x}'). \tag{24}$$

We seek the expression for $U(\nu;\mathbf{x},\mathbf{x}')$ in the following form:

$$U(\nu;\mathbf{x},\mathbf{x}') = \frac{e^{\Lambda(\mathbf{x})}}{(2\pi)^{3/2}} \int d^3p \exp\left[i\underline{p}(\mathbf{x}-\mathbf{x}') - \sigma_3 \sum_{k=1}^{3} iS_k p_k \nu + \frac{i\omega}{c} n_2(\omega;\mathbf{x})\nu \right]. \tag{25}$$

According to Eqs. (21) and (25), $\exp\Lambda(\mathbf{x})$ has to satisfy the following equation:

$$\left[\frac{\partial}{\partial \nu} + \sigma_3 \sum_{k=1}^{3} S_k \frac{\partial}{\partial x_k}; e^{\Lambda(\mathbf{x})} \right] - \frac{i\omega}{c}(n_2(\omega;\mathbf{x}) - \bar{n}_2)e^{\Lambda(\mathbf{x})} + \frac{I+\sigma_1}{2}\sigma_3 \sum_{k=1}^{3} S_k \frac{\partial}{\partial x_k} \ln\left(1 + \frac{n_2(\omega,\mathbf{x}) - \bar{n}_2}{\bar{n}_2}\right) e^{\Lambda(\mathbf{x})} = 0, \tag{26}$$

where the square bracket denotes the commutator:

$$[A;B] = AB - BA. \tag{27}$$

The relation (26) can be reduced, taking into account Eq. (2), to the linear equation for Λ

$$\left(I\frac{\partial}{\partial \nu} + \sigma_3 \sum_{k=1}^{3} S_k \frac{\partial}{\partial x_k} \right)\Lambda - \frac{i\omega}{c}\kappa(\omega)\frac{\delta N(\mathbf{x})\theta(x_1)}{\bar{N}} + \frac{I+\sigma_1}{2}\sigma_3 \sum_{k=1}^{3} S_k \frac{\partial}{\partial x_k} \ln\left(1 + \frac{\kappa(\omega)\delta N(\mathbf{x})\theta(x_1)}{\bar{N}\bar{n}_2}\right) = 0. \tag{28}$$

It follows from Eq. (28) that

$$\Lambda(\omega;\nu;\underline{x}) = \frac{1}{(2\pi)^{3/2}} \int e^{i\underline{q}\underline{x}} d^3q \left\{ \left[\frac{i\sigma_3}{q^2} \sum_{k=1}^{3} S_k q_k (I - e^{-i\nu\Sigma_{k=1}^{3}\sigma_3 S_k q_k}) + (I - \tilde{I}(q)\nu) \right] f(q) \right\}, \tag{29}$$

where

$$q = \sqrt{\mathbf{q}^2}, \quad f(q) = \frac{1}{(2\pi)^{3/2}} \int d^3x e^{-i\mathbf{q}\mathbf{x}} \times \left\{ \frac{i\omega}{c}\kappa(\omega)\frac{\delta N(\mathbf{x})\theta(x_1)}{\bar{N}} - \frac{I+\sigma_1}{2} \sum_{k=1}^{3} \sigma_3 S_k \frac{\partial}{\partial x_\kappa} \ln\left(1 + \kappa(\omega)\frac{\delta N(\mathbf{x})\theta(x_1)}{\bar{N}\bar{n}_2}\right) \right\}. \tag{30}$$

The exponent $\exp(-\mathrm{qi}\,\nu\Sigma_{k=1}^{3}\sigma_3 S_k q_k)$ in Eq. (29) can be rewritten as follows:

$$\exp\left[-i\nu \sum_{k=1}^{3} \sigma_3 S_k q_k \right] = I + (\cos\nu q - 1)\tilde{I}(q) - i\sum_{k=1}^{3} \sigma_3 S_k q_k \frac{\sin\nu q}{q}. \tag{31}$$

The matrix $\tilde{I}(q)$ in Eqs. (29) and (31) is defined by

$$\langle \alpha i|\tilde{I}(k)|\alpha j\rangle = \delta_{\alpha\beta}\left(\delta_{ij} - \frac{k_i k_j}{k^2}\right). \tag{32}$$

The expression (30) for Λ satisfies the following relations:

$$\frac{I+\sigma_1}{2}\Lambda(\omega;\nu;\mathbf{x})\frac{I+\sigma_1}{2} = \frac{I+\sigma_1}{2}\Lambda^*(\omega;\nu;\mathbf{x})\frac{I+\sigma_1}{2},$$

$$\frac{I+\sigma_1}{2}\left[\Lambda, I\frac{\partial\Lambda}{\partial\nu} + \sum_{k=1}^{3} \sigma_3 S_k \frac{\partial\Lambda}{\partial x_k} \right]\frac{I+\sigma_1}{2} = 0. \tag{33}$$

It follows from Eqs. (17), (18), (20), (25), (29), and (33) that

$$T(\ell)=\frac{LI_0}{(2\pi)^{3/2}(2\pi\sigma)^2}\left|\left\langle (F^0)^+\frac{I+\sigma_1}{2}\sigma_3\int_{|x_\parallel|<L}\delta(x_1)d^3xd^3x'\int d\omega n_1\right.\right.$$
$$\times\int d^3p\int_0^\infty d\nu\left\{\exp\left[-\frac{(|\omega|-\omega_0)^2}{\sigma^2}+i\frac{\omega}{c}\bar{n}_2(x_1'+\nu)-2i\frac{\omega}{c}n_1\ell+ip(\mathbf{x}-\mathbf{x}')+\Lambda(\mathbf{x})\right]\exp\left[-i\sigma_3\nu\sum_{k=1}^3 S_kp_k\right]\right.$$
$$\left.\left.\times\left[\frac{\omega}{c}\bar{n}_2(\omega)\kappa(\omega)\frac{\delta N(\mathbf{x}')\theta(x_1')}{\bar{N}}-\frac{I+\sigma_1}{2}\sum_{k=1}^3\sigma_3S_k\frac{\partial}{\partial x_k'}\ln\left(1+\frac{\kappa(\omega)\delta N(\mathbf{x}')\theta(x_1')}{\bar{N}}\right)\right]\right\}F^{(0)}\right\rangle\right|. \quad (34)$$

To simplify the calculations we suppose that the following quantity (ζ) is small:

$$(\zeta)=\exp-\frac{z^2}{2|\kappa|^2\left\langle\left(\frac{\delta N(\mathbf{x})}{\bar{N}}\right)^2\right\rangle}\ll 1 \quad \text{for } z\gtrsim 1. \quad (35)$$

Neglected in the following calculation are terms of the order of $(\zeta)<1$, which correspond to far tails of the fluctuation distribution of optical properties where random deviations from the applied Gaussian distribution law and irregular speckle effects become significant. The inequality (35) allow us to not impose the condition of non-negativity of $N(\mathbf{x})$ and make the following substitution:

$$\ln\left(1+\frac{\kappa\delta N(\mathbf{x})\theta(x_1)}{\bar{N}}\right)\to\kappa(\omega)\frac{\delta N(\mathbf{x})\theta(x_1)}{\bar{N}}. \quad (36)$$

After substitution (36) we find from Eq. (34) the following expression for $T(\ell)$:

$$T(\ell)=\frac{LI_0\,\mathrm{Re}}{(2\pi\sigma)^2}\left|\left\langle (F^0)^+\frac{I+\sigma_1}{2}\sigma_3\int_{|x_\parallel|<L}\delta(x_1)d^3x\int d\omega n_1\times\int d^3p\int_0^\infty d\nu\left\{\exp\left[-\frac{(|\omega|-\omega_0)^2}{\sigma^2}+i\mathbf{px}+i\frac{\omega}{c}\bar{n}_2\nu-2i\frac{\omega}{c}n_1\ell\right.\right.\right.$$
$$\left.\left.\left.+\Lambda(\underline{x})\right]\exp\left(-i\nu\sigma_3\sum_{k=1}^3S_k\tilde{p}_k\right)\left(\frac{i\omega}{c}\bar{n}_2-\sum_{k=1}^3 i\sigma_3S_k\tilde{p}_k\right)\frac{I-\sigma_1}{2}\delta n(\omega,\mathbf{p})\right\}F^0\right\rangle\right|;$$
$$\tilde{p}_k=p_k+\frac{\omega}{c}\bar{n}_2\delta_{k,1},$$
$$\delta n(\omega,\mathbf{p})=\kappa(\omega)\delta N(\mathbf{p}),$$
$$\delta N(\mathbf{p})=\frac{1}{(2\pi)^{3/2}}\int e^{-i\mathbf{px}}\frac{\delta N(\mathbf{x})}{\bar{N}}d^3x. \quad (37)$$

In transforming Eqs. (34)–(37), we have made the substitution

$$p_k\to p_k+\frac{\omega}{c}\bar{n}_2\delta_{k,l}$$

and taken into account Eq. (31) and the identity

$$\sigma_3S_1F^0=F^0. \quad (38)$$

The substitution (36) allows us also to present the $\Lambda(\omega;\nu;\mathbf{x})$ in the following form:

$$\Lambda(\omega;\nu;\mathbf{x})=\frac{1}{(2\pi)^{3/2}}\int e^{i\mathbf{qx}}\tilde{\Lambda}(\omega;\nu;\mathbf{q})\delta\eta(\omega',\mathbf{q})d^3q\Big|_{\omega'\to\omega} \quad (39)$$

with the matrix $\tilde{\Lambda}(\omega;\nu;\mathbf{q})$ equal to

$$\tilde{\Lambda}(\omega;\nu;\mathbf{q})=i\sigma_3\sum_{k=1}^3S_kq_k\left(\frac{i\omega}{c}\bar{n}_2\frac{1-\cos\nu q}{q^2}-\frac{I-\sigma_1}{2}\frac{\sin\nu q}{q}\right)$$
$$-\frac{i\omega}{c}\bar{n}_2\tilde{I}(q)\frac{\sin\nu q}{q}+\frac{I-\sigma_1}{2}\tilde{I}(q)(1-\cos\nu q)$$
$$+i\frac{\omega}{c}\bar{n}_2[I-\tilde{I}(q)]\nu. \quad (40)$$

In Eqs. (37) and (39) there enters the following Fourier transform $\delta\eta(\omega,\mathbf{q})$:

$$\delta\eta(\omega,\mathbf{q}) \equiv \frac{1}{(2\pi)^{1/2}}\int e^{i\omega t}\delta\eta(t,\mathbf{q})dt$$
$$= \frac{\kappa(\omega)}{(2\pi)^{3/2}}\int e^{-i\mathbf{q}\mathbf{x}}\frac{\delta N(\mathbf{x})}{\bar{N}}\theta(x_1)d^3x$$
$$= \frac{\kappa(\omega)}{(2\pi)^3}\int e^{i(\mathbf{q}'-\mathbf{q})\mathbf{x}}\delta N(\mathbf{q})e^{i\alpha x_1}\frac{d^3\mathbf{x}d^3\mathbf{q}'d\alpha}{\pi i(\alpha-i\varepsilon)}$$
$$= \frac{\kappa(\omega)}{i\pi}\int dq_1'\delta N(\tilde{\mathbf{q}})\left.\frac{1}{q_1'-q_1-i\varepsilon}\right|_{\varepsilon\to 0};$$

$$\tilde{q} = \{\mathbf{q}_{\|}, q_1'\}, \tag{41}$$

where $\delta N(\mathbf{q})$ is the Fourier transform of $\frac{\delta N(\mathbf{x})}{\bar{N}}$. The averaged-over fluctuations of $\delta N(\mathbf{x})$ functions of $\delta\eta(\mathbf{q},\omega)$ in the following calculations enter only under integrals over $d\omega$ and $d\mathbf{q}^{(1)}\cdots d\mathbf{q}^{(n)}$ with the integrands invariant under the inversion $d\mathbf{q}^{(n)}\to -d\mathbf{q}^{(n)}$, $\omega\to-\omega$ combined with a complex conjugation. This allows us to make the following substitution for the factor $[\pi i(q_1'-q_1-i\varepsilon)]^{-1}$ under the corresponding integrals in Eq. (41):

$$\frac{1}{\pi i}\frac{1}{q_1'-q_1-i\varepsilon}\to\frac{1}{2\pi i}\left(\frac{1}{q_1'-q_1-i\varepsilon}-\frac{1}{+q_1'-q_1+i\varepsilon}\right)$$
$$= \delta(q_1-q_1') \tag{42}$$

and to put $\delta\eta(\mathbf{q},\omega)$ equal to

$$\delta\eta(\mathbf{q},\omega)\to\kappa(\omega)\frac{1}{(2\pi)^{3/2}}\int e^{-i\mathbf{q}\mathbf{x}}\frac{\delta N(\mathbf{x})}{\bar{N}}d^3\mathbf{x} = \kappa(\omega)\delta N(\mathbf{q})$$
$$\equiv \kappa(\omega)\frac{1}{(2\pi)^3}\int e^{-i\mathbf{q}\mathbf{x}}\frac{\delta N(\mathbf{x})}{\bar{N}}d^3\mathbf{q}. \tag{43}$$

When averaging over fluctuations $\delta N(\mathbf{x})$ in a sample bulk we assume that the fluctuations are a stationary isotropic Gaussian random process defined by the basic moments [24]:

$$\langle\delta N(\mathbf{x})\rangle = 0,$$
$$\left\langle\frac{\delta N(\mathbf{x})\delta N(\mathbf{x}')}{\bar{N}^2}\right\rangle = D(\mathbf{x}-\mathbf{x}') = \Delta^2\exp\left(-\frac{(\mathbf{x}-\mathbf{x}')^2}{a^2}\right), \tag{44}$$

where Δ^2 characterizes the intensity of fluctuations in the volume with dimensions defined by the coherence length λ_c, with a being the correlation length. In the case of the noninteracting spherical particles with the radii R we have

$$\Delta^2 \cong \frac{1}{\bar{N}\lambda_c^3}, \quad a \cong \frac{1}{\sqrt[3]{\bar{N}}}. \tag{45}$$

It follows from Eqs. (31), (44), and (2) that

$$\langle\delta\eta(\omega,\mathbf{q})\rangle = 0,$$
$$\langle\delta\eta(\omega';\mathbf{q}')\delta\eta(\omega,\mathbf{q})\rangle = D(\omega';\mathbf{q}';\omega,\mathbf{q})$$
$$\equiv |\kappa(\omega)|^2\Delta^2(a\sqrt{\pi})^3e^{-q^2a^2/4}$$
$$\times\delta_{-\omega';\omega}\delta^3(\mathbf{q}'+\mathbf{q})$$
$$= D(\omega,\mathbf{q})\delta_{-\omega',\omega}\delta^3(\mathbf{q}+\mathbf{q}'). \tag{46}$$

The factor $\delta_{-\omega',\omega}$ in Eq. (46) follows from the time-dependence of the correlator $\langle\delta\eta(t';\mathbf{q}')\delta\eta(t;\mathbf{q})\rangle$ only on the difference $t'-t$ [25]. The description of the averaging in expression (37) for $T(\ell)$ is given in Appendix A, where the expression (A7) for $T(\ell)$ is presented in the form of a double integral over $d\omega$ and $d\nu$. The integral over $d\omega$ in Eq. (A7) can be taken (as is usually done in wave-packet descriptions) in the asymptotic approximation with the following result:

$$T(\ell) = \frac{\pi I_0L^3\Delta^2n_1}{2^{5/2}\sigma}|\kappa(\omega_0)|^2\,\mathrm{Re}\int_0^\infty d\nu\times\exp\left[-\frac{2\omega_0}{c}\nu\,\mathrm{Im}\,\bar{n}_2(\omega_0)-g(\omega_0,\nu)\right]\left\{f_+(\omega_0,\nu)\times\exp-\left[\frac{\sigma^2}{c^2}(\nu\,\mathrm{Re}\,\bar{n}_2(\omega_0)-\ell n_1)^2\right]\right.$$
$$\left.\times\exp 2i\frac{\omega_0}{c}(\nu\,\mathrm{Re}\,\bar{n}_2(\omega_0)-\ell n_1)+f_-(\omega_0,\nu)\exp-\left[\left(\frac{\sigma\ell}{c}\right)^2+2i\frac{\omega_0}{c}n_1\ell\right]\right\}, \tag{47}$$

where definitions of the functions $g(\omega,\nu)$ and $f_\pm(\omega,\nu)$ are given in Eqs. (A2) and (A8). In the derivation of Eq. (47), we have taken into account the invariance of the integrand in Eq. (A8) under complex conjugation with simultaneous substitution $\omega\to-\omega$ and for simplicity we do not take into account explicitly the effects of frequency dispersion in $g(\omega,\nu)$ and $f\pm(\omega,\nu)$. These effects lead to the substitution in Eq. (47) of the group velocities for the phase ones:

$$\frac{c}{n(\omega)}\to c\left.\frac{1}{\frac{\partial|\omega n(\omega)|}{\partial\omega}}\right|_{\omega=\omega_0}. \tag{48}$$

In the considered experiments, where $n(\omega)$ varies relatively slowly in the frequency interval $\omega_0\pm\sigma$, and the particle concentration is relatively low, the disregarded dispersion effects are unimportant.

The remaining integral over $d\nu$ in Eq. (47) can be taken in the asymptotic (stationary phase) approximation since we have supposed that the considered values of ℓ satisfy the inequality

$$\left(\frac{\sigma}{c}\ell\right)^2 \gg 1.$$

This inequality allows us to separate and exclude from consideration surface effects. We find after asymptotic integration over $d\nu$ that

$$T(\ell) = \frac{\pi^3 I_0 L^3 \Delta^2 n_1 c}{2^{5/2}\sigma^2 \operatorname{Re}\bar{n}_2(\omega)} |\kappa(\omega_0)|^2 e^{-\omega_0^2/\sigma^2} \times \left\{ \exp\left[-\frac{\omega_0}{c}\tilde{\ell} \operatorname{Im}\bar{n}_2(\omega_0) - g(\omega_0,\tilde{\ell}) \right] \times \operatorname{Re} f_+(\omega_0,\tilde{\ell}) \right\}; \quad \tilde{\ell} = \ell \frac{n_1(\omega_0)}{\operatorname{Re}\bar{n}_2(\omega_0)}. \tag{49}$$

In Eq. (49), we have supposed that

$$\frac{(\operatorname{Im} n_1(\omega_0))^2}{(\operatorname{Re} n_1(\omega_0))^2} \ll 1.$$

The structure of the exponential factor in Eq. (49) deserves special attention. It is equal to

$$\exp\left[-\frac{\omega_0}{c}\tilde{\ell} \operatorname{Im}\bar{n}_2(\omega) - g(\omega_0,\tilde{\ell}) \right],$$

where $g(\omega_0,\tilde{\ell})$, according to Eq. (A2), is proportional to $\frac{1}{3}|\kappa(\omega_0)\Delta|^2\left(\frac{\omega_0}{c}\tilde{\ell}\right)^2$ for the larger $\tilde{\ell} \gg a$. Such quadratic dependence on $\tilde{\ell}$ for the wave-packet decomposition and the light intensity distribution homogenization is dominating at large $\tilde{\ell}$. It is characteristic for diffusion processes [5,4] with the effective light diffusion coefficient D proportional to

$$D \sim \frac{\sigma}{\left(\frac{c\Delta}{\bar{n}\omega}\sum_\beta \bar{N}_\beta A_\beta(0)\right)^2}. \tag{50}$$

In the estimation (50) we have used Eq. (3) and performed a Fourier transform over ω to find the signal time dependence. Note the dependence of the experimentally measured quantities on the wave-packet width σ and L_c. Analogous dependences were previously discussed in [27].

IV. COMPARISON OF EXPERIMENTAL DATA WITH THEORY

We will compare theory with experimental measurements in the interval

$$\frac{c}{\sigma} < \tilde{\ell} < \tilde{\ell}_m,$$

where $\tilde{\ell}_m$ corresponds to the value of $\tilde{\ell}$ after which the backscattering signal becomes undistinguishable from the background. In the realized experimental results with relatively low particle concentrations, we have, for relatively small $\tilde{\ell}$ and R,

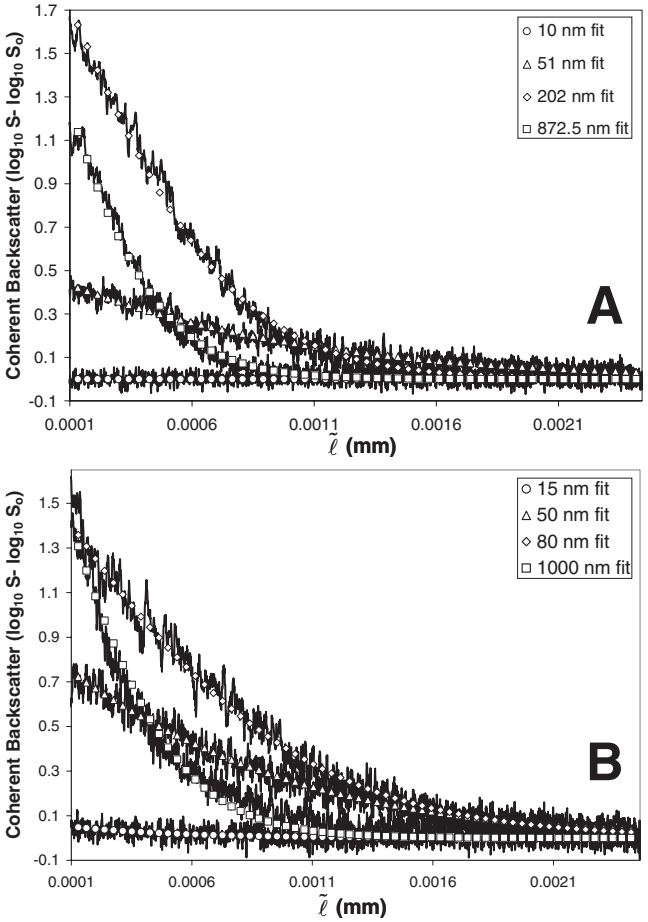

FIG. 6. Plot of representative sample decay profiles with accompanying nonlinear least-squares fit. Decay profiles for several 0.01 volume fraction samples are shown in (A). Decay profiles for the 0.10 volume fraction samples are shown in (B). Note that signal fluctuation intensities can be qualitatively seen to vary proportionally with mean particle radius.

$$g(\omega_0,\tilde{\ell}_m) \ll \frac{\omega_0}{c}\tilde{\ell}_m \operatorname{Im}\bar{n}_2(\omega_0). \tag{51}$$

To avoid excessively cumbersome expressions in our derivations, we have neglected corresponding terms with $g(\omega_0,\ell)$ in Eq. (49) and other subsequent equations.

According to our theoretical model, the averaged experimental signals $S(\tilde{\ell})$ presented in Figs. 4 and 5 must have the following form for small $\tilde{\ell}$ and R:

$$\log_{10} S(\ell) - \log_{10} S_0 \equiv \log_{10}\frac{S(\ell)}{S_0} = \log_{10}(1 + CA(\tilde{\ell})e^{-B\tilde{\ell}}), \tag{52}$$

where S_0 is the background signal and when Eqs. (51) and (52) hold

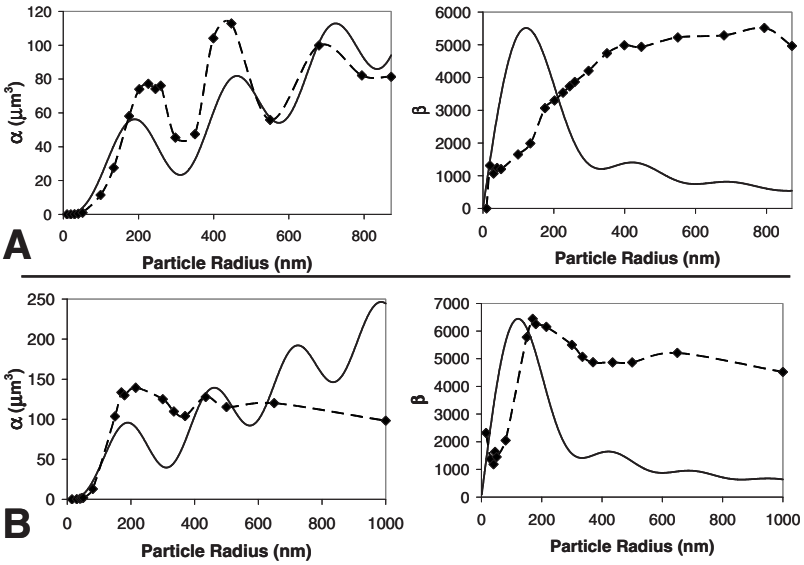

FIG. 7. Plot of fitting parameters obtained by fitting experimental data (dashed lines) with theoretical expressions for the same parameters from Mie theory (solid lines). (A) The α and β terms for the 0.01 volume fraction sample and (B) the α and β terms for the 0.10 volume fraction sample. As explained in Sec. IV, because we have neglected terms with $g(\omega_0,\ell)$ from Eq. (49), the expression for β used to calculate the presented theoretical values is only valid for relatively small values of R.

$$A(\tilde{\ell}) = \mathrm{Re}\, f(\omega_0,\tilde{\ell})\frac{|\kappa(\omega_0)|^2\Delta^2}{\mathrm{Re}\,\bar{n}_2(\omega_0)},$$

$$B = \frac{\omega_0}{c}\,\mathrm{Im}\,\kappa(\omega_0). \tag{53}$$

The constant C in Eq. (52) characterizes the experimental device response and is independent of the individual sample properties. The expression for $\tilde{\ell}$ is given in Eq. (49) and all other functions entering Eq. (53) are described in the Appendixes A and B.

The expression (52) was fit to the experimental data using a nonlinear least-squares algorithm from the curve-fitting toolbox of MATLAB (The MathWorks Inc., Natick, MA), with representative decay profiles with their corresponding fits shown in Fig. 6. We then extracted values for the $|\kappa(\omega_0)|^2$ and Im $\kappa(\omega_0)$ in Eq. (53) from the fit of the experimental data, which we will refer to as α and β, respectively. The parameters α and β, which are related to overall backscatter intensity and the rate at which backscatter intensity decreases as a function of ℓ, can also be derived from theoretical concerns set forth in Appendix B. Figure 7 contains a comparison of theoretical and experimental values obtained as α and β as a function of particle radius.

The experiments performed elucidate the signal dependence on the particle radii $R=R_\beta$ for samples with constant particle volume fraction $\rho=\rho_\beta=$const. As seen in Figs. 6 and 7, the dependence of the experimental signal on $\tilde{\ell}$ and the values of α and β on R reasonably fit the theoretical expressions. A preliminary description of these experimental data has been given previously in [28]. The dependence on R shown in Fig. 7 reproduced the general shape of Mie resonances. The differences between detailed experimental and theoretical curves can be attributed to differences between real particle structures and their uniformity supposed in Mie theory, as well as to our application of an approximation to Mie theory. In Fig. 8, we see a comparison of the α terms for the 0.01 and 0.10 volume fraction sample series. The position of the Mie resonances do not shift with the changing particle concentration and depend mostly on the light scattering characteristics of individual particles, while the intensity of the resonances varies with sample concentration. This allows us to separate information about the particle density and individual particle characteristics, including adsorption, in both monodisperse and polydisperse particle suspensions.

It is also worth noting that the factor Δ^2, which enters in expression (53) for $A(\tilde{\ell})$, decreases with increasing particle concentration $\bar{N}$ and coherence length λ_c, which is accompanied with decreasing fluctuation effects. An analysis of signal intensity fluctuations (Fig. 9) shows that they are much larger than the optical polarization fluctuation in the uniform polar media [29]. While not entirely deconvoluted from instrumental noise, the fluctuations are obviously related to nonuniformities of the particle space distribution, as characterized by

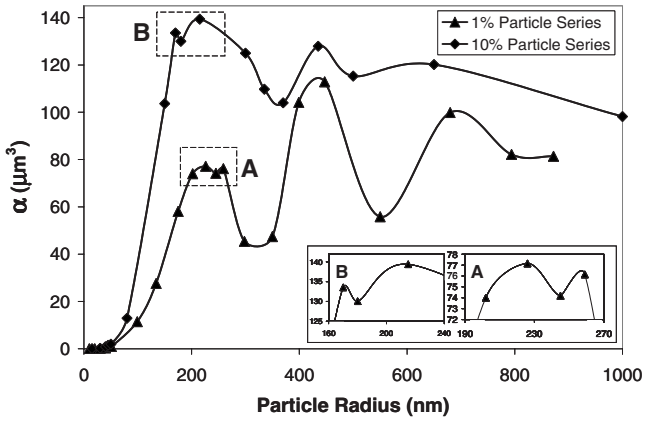

FIG. 8. Comparison of the α fitting parameter for the 0.01 and 0.10 volume fraction sample sets. The Mie resonance maxima occur at the same particle radius regardless of sample concentration, allowing the deconvolution of particle density and particle scattering characteristics. Highlighted in the inset are two reproducible anomalies in signal intensity observed near the first Mie resonance maximum in both sample sets. We attribute this increase in intensity to surface-enhanced inelastic scattering events.

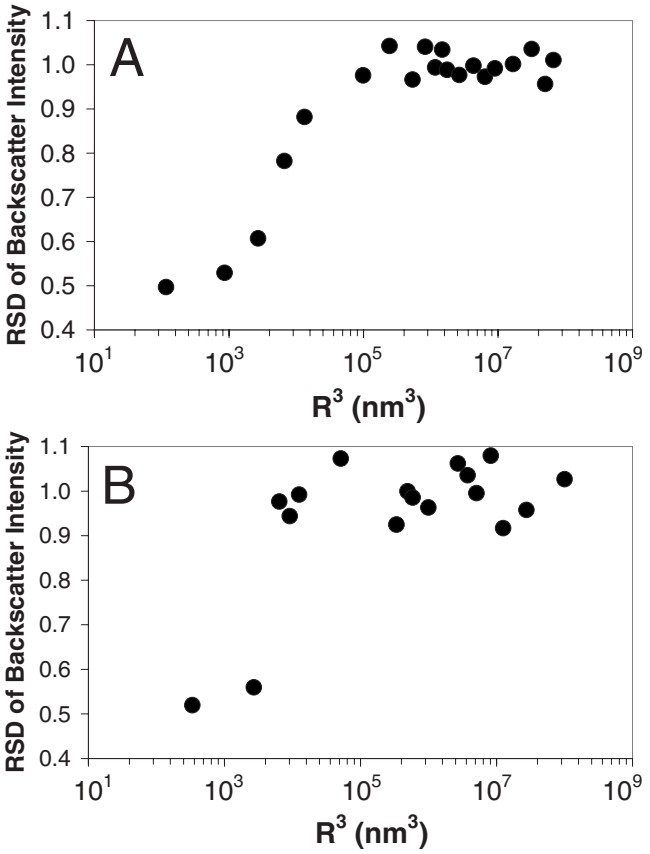

FIG. 9. Analysis of signal fluctuations. (A) and (B) are, respectively, the relative standard deviation (RSD) of the coherent backscatter signal near the beginning of the decay profiles of the 0.01 and 0.10 volume fraction samples. The fluctuations are a convolution of instrumental noise and signal changes caused by Brownian motion of the particles in the matrix. A general trend of increasing fluctuation intensity with increasing particle radius is observed.

Δ^2. The factor Δ^2 and corresponding fluctuations have to increase according to Eq. (45) with increasing particle radii at the same volume concentration (i.e., decreasing particle number per unit volume). Such general dependence was observed in the experiments, with the indication of self-assembly effects in the case of the smallest particle radii.

V. CONCLUSION

We have described experiments of light backscattering by nonuniform particle containing media. The theory of the corresponding effects was developed in the framework of classical linear electrodynamics. The calculations were based on the introduction of the effective dielectric function and a fifth additional coordinate followed by functional integral averaging. Gaussian averaging is adequate in the case of an equilibrium distribution of weakly interacting particles, as well as in the case of freely diffusing particles in liquids far from critical points [25]. It may be possible to generalize our calculations to more complex cases of quasi-Gaussian distributions. By changing the expression for the kernel $D(\mathbf{x}-\mathbf{x}')$ in Eq. (44), it is relatively simple to generalize these results to cases of Poissonian distributions or finite sums of different Gaussian distributions with different correlation lengths. More complicated but feasible are calculations with the kernel describing particle distribution correlations for charged colloids.

The expression (50) for the light diffusion coefficient D also allows us to estimate the Thoules time $T_{\mathrm{Th}} \sim \frac{\ell_{\mathrm{mp}}^2}{D}$ after which localization effects in multiscattering media can cause deviations of wave-packet destruction from the decay law, with linear dependence of the exponent on ℓ [26].

Note that coherent scattering by randomly oriented and distributed nonspherical and polarizable scatterers such as polycrystals and liquid crystals does not require a qualitatively different treatment. As was shown by Placzek, the cross sections of incoherent light scattering by the freely oriented systems can contain three independent parts: scalar, antisymmetric, and symmetric [30]. However, the cross sections of coherent scattering contain only a scalar part and thus the effective dielectric function introduced in Eqs. (2) and (3) for the description of the considered coherence effect remains a scalar with nonscalar effects contributing to an effective light absorption.

The effects of nonscalar scattering components can, in principle, be separated and measured by the modification of the considered techniques by imposing external fields on a studied sample containing randomly distributed orientable or polarizable particles [31], then measuring the signal dependence on the angle between the light polarization and the external field. The analogous effect was observed in [32] in studying light backscattering from orientationally ordered liquid crystals. Optically active media can be characterized by comparing the results of coherent backscattering of light with the opposite circular polarizations [33]. As was stated before, these specific effects are expected in the cases where the anomalous dispersion effects are important.

The appearance of Mie-type resonances in our work is of special interest. Such effects are the result of large electromagnetic field increases near nanoparticle boundaries in the Mie resonance frequency interval, and such field increases can lead to an enhancement of optical transitions and to changes of absorption characteristics [34]. A recent publication described substantial amplification of Raman scattering in the resonance frequency interval for molecules adsorbed on silicon nanocones and nanowires [35]. In the relatively simple system considered in our work, the analogous effect can be much more pronounced with much larger boundary surface area of spherical nanoparticles, and the results could be relatively simply predicted and interpreted with the help of Mie's analytical formulas. In particular, we have observed small anomalous increases in particle scattering intensity, as shown in the insets of Fig. 8, which we believe can be explained as a result of a resonance scattering effect. The light frequency in our experiments corresponds to the wavelength region near Raman transitions corresponding to intramolecular transitions in water molecules [36]. In addition to Raman scattering, other enhanced optical transitions and electron photoemission effects could be observed. The possibility of the enhancement of electromagnetic transitions near the surface of semiconducting and insulating nanoparticles is note-

worthy for a number of optoelectronic applications, adsorption studies, and the construction of sensitive analytical devices.

The proposed theoretical approach can be applied for the description of a number of different wave propagation effects in nonuniform media, in particular the description of mirrorless lasing in random gain media, fluctuational waveguiding, memory, and light trapping effects. The described experimental technique and its modifications may be useful for *in situ* monitoring of the fast dynamics of such important processes as polymerization, gelation, phase transitions, coagulations, and nucleation in colloids, dispersals, and aerosols. The considered detection technique is also well-suited for the screening and sorting of various metallic and nonmetallic nanoscale particles including viruses and larger proteins, in low concentration solutions. As mentioned at the end of Appendix B, the considered optical technique also opens intriguing possibilities of studying interface water solution properties.

ACKNOWLEDGMENTS

This research was supported by the U. S. Department of Energy Environmental Management Science Program under Grant No. 81964 and the Center for Process Analytical Chemistry.

APPENDIX A: AVERAGING

We will follow the rules of quasi-Gaussian averaging [1,19,20]. According to these rules and Eq. (46)

$$\left\langle \delta\eta(\omega^{(1)},\mathbf{q}^{(1)})\cdots\delta\eta(\omega^{(n)},\mathbf{q}^{(n)})\exp\int O(\omega,\mathbf{q})\delta\eta(\omega,\mathbf{q})\right\rangle = \frac{\delta^n}{\delta\alpha(\omega^{(1)},\mathbf{q}^{(1)})\cdots\delta\alpha(\omega^{(n)},\mathbf{q}^{(n)})} \times\exp\left\{\frac{1}{2}\int d^3q\times[\alpha(-\omega,-\mathbf{q})O(-\omega,-\mathbf{q}) \times D(\omega,\mathbf{q})O(\omega,\mathbf{q})\alpha(\omega,\mathbf{q})]\right\}\Bigg|_{\alpha(\omega^n,\mathbf{q}^{(n)})=1}, \tag{A1}$$

where $\frac{\delta}{\delta\alpha(\omega^{(n)},\mathbf{q}^n)}$ denotes the functional derivative. In our problem, the operator $D(\omega,\mathbf{q})$ is defined by Eq. (46) and the operator $O(\omega,\mathbf{q})$ is expressed through the matrix $\tilde{\Lambda}(\omega,\mathbf{q})$ introduced in Eq. (40). Equation (A1) can be verified by a series expansion of the exponent followed by term-by-term averaging according to Gaussian rules with a subsequent summation of the averaged terms. According to these rules, the mean values of the products of odd numbers of factors $\delta\eta(\omega,\mathbf{q})$ are equal to zero and the mean values of the products of even numbers of $\delta\eta(\omega,\mathbf{q})$ are reduced to products of all their possible pair correlators by the Wick theorem.

We start by a calculation of the quantity $g(\omega,\nu)$:

$$g(\omega,\nu)=-\frac{|\kappa(\omega)|^2\Delta^2a^3}{(2\pi)^{3/2}}\times\frac{I+\sigma_1}{2}\int e^{-q^2a^2/4}|\tilde{\Lambda}(\omega,\nu,\mathbf{q})|^2d^3q=-\frac{|\kappa(\omega)|^2\Delta^2a^3}{(2\pi)^{3/2}} \times\frac{I+\sigma_1}{2}\,\mathrm{Re}\int e^{-q^2a^2/4}d^3q\left\{\left[\sum_{k=1}^{3}i\sigma_3S_kq_k\left(\frac{i\omega}{c}\frac{1-\cos\nu q}{q^2}+\frac{I-\sigma_1}{2}\frac{\sin\nu q}{\bar{n}_2q}\right)-\frac{I-\sigma_1}{2}\tilde{I}(q)(1-\cos\nu q)\right.\right.$$
$$\left.-\frac{i\omega\bar{n}_2(\omega)}{c}\tilde{I}(q)\frac{\sin\nu q}{q}+\frac{i\omega}{c}(I-\tilde{I}(q)\nu)\right]\times\left[\sum_{k=1}^{3}i\sigma_3S_kq_k\left(\frac{i\omega}{c}\frac{1-\cos\nu q}{q^2}-\frac{I-\sigma_1}{2}\frac{1}{\bar{n}_2}\frac{\sin\nu q}{q}\right)+\frac{I-\sigma_1}{2\bar{n}_2}\tilde{I}(q)(1-\cos\nu q)\right.$$
$$\left.\left.-\frac{i\omega\bar{n}_2(\omega)}{c}\tilde{I}(q)\frac{\sin\nu q}{q}+\frac{i\omega}{c}(I-\tilde{I}(q))\nu\right]\right\}=\frac{I+\sigma_1}{2}\frac{|\kappa(\omega)\Delta|^2a^3}{(2\pi)^3}\int e^{-a^2q^2/4}d^3q\left\{\frac{2}{3}\frac{\omega^2n_2(\omega)}{c^2}\frac{(1-\cos\nu q)}{q^2}+\frac{2}{3}\frac{i\omega}{c}\times\frac{\bar{n}_2}{|\bar{n}_2|^2}(1\right.$$
$$\left.-\cos\nu q)\frac{\sin\nu q}{q}+\frac{2}{3}\frac{\omega^2n_2^2(\omega)}{c^2}\frac{(\sin\nu q)^2}{q^2}+\frac{1}{3}\frac{\omega^2n_2^2(\omega)}{c^2}\nu^2\right\}=\frac{I+\sigma_1}{2}\frac{|a\kappa(\omega)\Delta|^2}{2}\left[\frac{4}{3}(1-e^{-\nu^2/a^2})\frac{\omega^2}{c^2}n_2^2(\omega)+\frac{2}{3}\frac{\omega^2n_2^2(\omega)}{c^2}\frac{\nu^2}{a^2}\right.$$
$$\left.+\frac{2\nu}{a^2}\frac{i\omega n_2(\omega)}{c}(e^{-\nu^2/a^2}-e^{-4\nu^2/a^2})\right]\equiv\frac{1+\sigma_1}{2}\tilde{g}(\omega,\nu);$$

$$\tilde{g}(\omega,\nu)=|\kappa(\omega)\Delta|^2\left(\frac{n_2(\omega)\omega}{c}\nu\right)^2\times\begin{cases}1 & \text{for } \nu\ll a\\ \frac{1}{3} & \text{for } \nu\gg a.\end{cases} \tag{A2}$$

In Eq. (A2) we have used the definition in Eq. (40) of $\tilde{\Lambda}$ and Eq. (46).

The second quantity $r(\omega,\mathbf{p})$ which enters in the expression for $T(\ell)$ is equal to

$$r(\omega,\underline{p}) = \left. \frac{I+\sigma_1}{2(2\pi)^3} e^{i\mathbf{px}} \langle \delta\eta(p,\omega)\Lambda(\omega',\nu,\mathbf{x}) \rangle \right|_{\omega'=\omega} = \frac{I+\sigma_1}{2^{5/2}} |\kappa(\omega)\Delta|^2 \tilde{\Lambda}(-\omega;\nu,-\mathbf{p}) e^{-p^2a^2/4}. \tag{A3}$$

Note that both quantities (A2) and (A3) do not depend on x.

It follows from Eqs. (37) and (A1)–(A3) that

$$T(\ell) = \frac{L^3 I_0}{4\pi\sigma^2} \mathrm{Re} \int d^3p \int_{-\infty}^{\infty} n_1(\omega) d\omega \int_0^{\infty} d\nu e^{-p^2a^2/4} \times \left\{ \exp\left[-\frac{(\omega-\omega_0)^2}{\sigma^2} + \frac{i\omega}{c}\bar{n}_2(\omega)\nu - 2i\frac{\omega}{c}n_1(\omega)\ell - g(\omega,\nu) \right] \right.$$
$$\left. \times \left\langle (F^{(0)})^+ \frac{I+\sigma_1}{2} \frac{r(-\omega,-\mathbf{p}) + r(\omega,\mathbf{p})}{2} \exp\left[-i\nu\sigma_3 \sum_{k=1}^{3} S_k \tilde{p}_k \right] \left[\frac{i\omega}{c}\bar{n}_2 - \frac{1}{2}\sum_{k=1}^{3} i\sigma_3 S_k \tilde{p}_k \right] \frac{I-\sigma_1}{2} F^{(0)} \right\rangle \right\},$$

$$\tilde{p}_k = p_k + \frac{\omega}{c}\bar{n}_2(\omega)\delta_{k,1}. \tag{A4}$$

The matrix structure of Eq. (A4) can be resolved by taking into account the identities

$$\sigma_3 S_1 F^{(0)} = F^0,$$

$$(F^0)^+ \sigma_3 S_{2,3} F^0 = 0, \tag{A5}$$

with the following result:

$$T(\ell) = -\frac{I_0 L^3 \Delta^2}{2^{7/2}\sigma^2} \int_{-\infty}^{\infty} e^{-p^2a^2/4} dp \int_{-1}^{1} dz \int_{-\infty}^{\infty} d\omega n_1(\omega) |\kappa(\omega)|^2 \times \frac{i\omega}{c} \int_0^{\infty} d\nu \left\{ \exp\left[i\frac{\omega}{c}\bar{n}_2(\omega)\nu - 2\frac{i\omega}{c}n_1(\omega)\ell - g(\omega,\nu) \right.\right.$$
$$\left.\left. - \frac{(|\omega|-\omega_0)^2}{\sigma^2} \right] pz \left[ip\sin p\nu + \frac{\omega}{c}\bar{n}_2(\omega)(\cos p\nu - 1) \right] \frac{1}{\nu}\frac{\partial}{\partial\nu}\nu\frac{\partial}{\partial\nu}\frac{\sin\nu\tilde{p}}{\tilde{p}} \right\},$$

$$\tilde{p} = \sqrt{p^2 + 2pz\frac{\omega}{c}\bar{n}_2 + \left(\frac{\omega}{c}\bar{n}_2\right)^2}. \tag{A6}$$

After integration in Eq. (A6) over dz and integration by parts over $d\nu$ we find from Eq. (A5) that

$$T(\ell) = \frac{I_0 L^3 \sqrt{\pi}}{2^{3/2}\sigma^2} \int_{-\infty}^{\infty} \frac{d\omega |\kappa(\omega)|^2}{\frac{\omega}{c}\bar{n}_2(\omega)} \frac{n_1}{\bar{n}_2(\omega)} \exp - \left[\frac{(|\omega|-\omega_0)^2}{\sigma^2} + 2i\frac{\omega}{c}n_1\ell \right] \times \int_0^{\infty} e^{-p^2a^2/4} dp \int_0^{\infty} d\nu F_1(\nu,p) \frac{\partial}{\partial\nu}\left(\nu\frac{\partial}{\partial\nu}F_2(\nu,p) \right),$$

where

$$F_1(\nu,p) = \frac{1}{\nu}\left[\cos p\nu \cos\frac{\omega}{c}\bar{n}_2\nu + \frac{1}{\nu^2 p\frac{\omega}{c}\bar{n}_2} \sin\nu p \sin\frac{\omega}{c}\bar{n}_2\nu - \frac{1}{\nu^2\frac{\omega}{c}\bar{n}_2} \cos\nu p \sin\frac{\omega}{c}\bar{n}_2\nu - \frac{1}{\nu p}\sin\nu p\cos\frac{\omega}{c}\bar{n}_2\nu \right],$$

$$F_2(\nu,p) = \frac{1}{\nu}\exp\left[i\frac{\omega}{c}\bar{n}_2\nu - \tilde{g}(\omega,\nu) \right] \times \left[ip\sin\nu p + \frac{\omega}{c}\bar{n}_2(\cos p\nu - 1) \right].$$

The integration over dp in the expression for $T(\ell)$ can be made analytically with the following result:

$$\frac{I_0 L^3 \Delta^2 \pi}{2^{5/2} a\sigma^2} \int_{-\infty}^{\infty} |\kappa(\omega)|^2 \frac{n_1}{\bar{n}_2(\omega)} d\omega \int_0^{\infty} d\nu \exp - \left[\tilde{g}(\omega,\nu) + \frac{(|\omega|-\omega_0)^2}{\sigma^2} \right]$$
$$\times \left\{ f_+(\omega,\nu)\exp\left[2i\frac{\omega}{c}(\nu\bar{n}_2(\omega) - \ell n_1) \right] + f_-(\omega,\nu)\exp - \left[2i\frac{\omega}{c}n_1\ell \right] \right\}. \tag{A7}$$

The functions $f_{\pm}(\omega,\nu)$ are rather complicated. However, for comparison with experimental data we need only the limits where $\nu > \frac{c}{\omega_0\bar{n}_2}$,

$$f_{\pm}(\omega,\nu)=f^{*}(-\omega,\nu)=\left\{\left[\left(\frac{\omega}{c}\bar{n}_2\right)^2(1-2e^{-\nu^2/a^2})+\frac{6}{a^2}\right]\times\left(1\mp\frac{1}{i\frac{\omega}{c}\bar{n}_2\nu}\right)+\frac{i}{\nu}\left(3\frac{\omega}{c}\bar{n}_2+\frac{2}{a^2\frac{\omega}{c}\bar{n}_2}\right)\right\}\left[1+O\left(\frac{a^2\left(\frac{\omega}{c}\bar{n}_2\right)^{-2}}{\nu^2}\right)\right]. \tag{A8}$$

In Eq. (A8) we have taken into account that according to Eq. (A2)

$$\frac{\partial}{\partial\nu}\frac{1}{\nu}\frac{\partial}{\partial\nu}\tilde{g}(\nu)\to 0 \quad \text{for } \nu<a$$

and dropped the small terms proportional to the derivatives of $\tilde{g}^2(\nu)$.

In the case of small ν we have

$$f_{\pm}(\omega,\nu)=\frac{8}{a^3}\left(\frac{\omega}{c}|\bar{n}_2|\nu\right)^2\left[1+O\left(\frac{\omega}{c}|\bar{n}_2|\nu\right)\right]. \tag{A9}$$

The function $f_{+}(\omega,\nu)\exp-[2\,\mathrm{Im}\,\bar{n}_2\nu]$ has the maximum at ν equal approximately to ν_m, where

$$\nu_m\sim\frac{1}{\mathrm{Im}\,\bar{n}_2}. \tag{A10}$$

APPENDIX B: EXPRESSION FOR THE COEFFICIENT $\kappa(\omega)$

According to Eq. (3), to evaluate $\kappa(\omega)$ it is necessary to choose an expression for the forward scattering amplitude $A_\beta(0)$ in the single particle scattering regime. In the considered experiments the refractive indices of media and particles, n_m and n_p, do not substantially differ from each other and the following inequality holds:

$$\gamma^2<1 \quad \text{for } \gamma=\frac{n_p-n_m}{n_m}. \tag{B1}$$

In such a case, it is possible to describe light scattering by uniform spheres with the van de Hulst approximation to the Mie solution [18,20], according to which

$$A_\beta(0)=i\frac{\omega}{c}n_mR_\beta^2\left[\frac{1}{2}+\frac{i}{y}e^{iy}-\frac{1}{y^2}(e^{iy}-1)\right],$$

$$y=2\frac{\gamma\omega\bar{n}_m}{c}R_\beta. \tag{B2}$$

The expression (B2) provides, with the accuracy defined by condition (B1), the correct limits both for small [Eq. (5)] and large [Eq. (6)] radius limits for Mie theory if we substitute in Eq. (B2),

$$\gamma\to\frac{3}{2}\frac{n_p^2-n_m^2}{n_p^2+2n_m^2}.$$

In this case we get the exact expression in the small radius limit and at the same time retain correct expressions for $A_\beta(0)$ for larger R_β up to terms of the higher relative order of γ^2.

In Mie calculations, the parameter γ defines the boundary condition at a particle-medium interface with a jump across the boundary of the normal component of the vector potential. In our experiments, particles are surrounded by a narrow flexible dipole boundary layer and an electrochemical double layer (both atomic dimensions are much less than the wavelength of incident light) responsible for the repulsion between particles. Both of these layers can contribute to the above-mentioned jump. At the particle-solvent interface the potential drop at atomic distances can reach 0.1–2.0 V. Therefore dielectric properties and the boundary condition for an electric field at the particle interface can be substantially altered.

Correspondingly we consider γ in the comparison with experiment as an adjustable parameter which characterizes the structure of the particle-medium interface, in this work found to be

$$\gamma=1.85\pm0.1. \tag{B3}$$

The value of γ can also depend on the specific structure of water molecules near the boundary of the sample. Such dependence opens the interesting possibility of studying the statistical and dynamic behavior of interfacial water, which is of great importance for the understanding of many physical, chemical, and biological phenomena [37]. It follows from Eqs. (3) and (B2) that for monodisperse samples with spherical particles we have the following expressions for $|\kappa(\omega)|^2$ and Im $\kappa(\omega)$:

$$|\kappa(\omega)|^2=\frac{8}{R_\beta^2}\left(\frac{c\rho_\beta}{\omega\bar{n}_m}\right)^2\left[\frac{1}{4}+\frac{1}{y^2}-\left(\frac{2}{y^4}+\frac{1}{y^2}\right)(\cos y-1)-\frac{\sin y}{y}\left(1+\frac{2}{y^2}\right)\right]\to 4\gamma^2\rho_\beta^2 \quad \text{for } y<1;$$

$$\mathrm{Im}\,\kappa(\omega)=\frac{3\rho_\beta}{R_\beta\frac{\omega}{c}\bar{n}_m}\left(\frac{1}{2}+\frac{1-\cos y}{y^2}-\frac{\sin y}{y}\right)$$

$$\to\frac{3}{2}\frac{\omega}{c}\bar{n}_mR_\beta\gamma^2\rho_\beta \quad \text{for } y<1. \tag{B4}$$

[1] K. Watson, J. Math. Phys. **10**, 688 (1969).
[2] D. De Wolf, IEEE Trans. Antennas Propag. **19**, 254 (1971).
[3] *New Aspects of Electromagnetic and Acoustic Wave Diffusion*, edited by POAN Research Group, Springer Tracts in Modern Physics Vol. 144 (Springer-Verlag, Berlin, 1998).
[4] *Scattering and Localization of Classical Waves in Random Media*, edited by P. Sheng (World Scientific, London, 1990). The latest work on localization of electromagnetic waves in random media has been summarized in S. Balog, P. Zakharov, F. Scheffold, and S. E. Skipetrov, Phys. Rev. Lett. **97**, 103901 (2006).
[5] M. van Rossum and T. Nieuwenhyzien, Rev. Mod. Phys. **71**, 313 (1999).
[6] P. de Vries, D. van Coevorden, and A. Langendijk, Rev. Mod. Phys. **70**, 447 (1998).
[7] V. Apalkov, M. Raikh, and B. Shapiro, J. Opt. Soc. Am. B **21**, 132 (2004).
[8] A. Kalugin, A. Bronshtein, and R. Mazar, Waves Random Media **14**, 389 (2004), and references therein.
[9] D. J. van Manen, J. O. A. Robertsson, and A. Curtis, Phys. Rev. Lett. **94**, 164301 (2005).
[10] Y. Kuga and A. Ishimaru, J. Opt. Soc. Am. A **8**, 831 (1984); M. P. Van Albada and A. Lagendijk, Phys. Rev. Lett. **55**, 2692 (1985); P. E. Wolf and G. Maret, *ibid.* **55**, 2696 (1985). The effect of backscattering enhancement for porous media containing small MgO particles was reported much earlier by B. Lyot, Ann. Obs. Paris **8**, 7 (1929).
[11] I. Dodd and I. McCarthy, Phys. Rev. **134**, A1136 (1964).
[12] The seminal work in applications of light scattering for random media diagnostics was performed by P. Debye and A. Bueche, J. Appl. Phys. **20**, 518 (1949). For more recent works see F. V. Ignatovich and L. Novotny, Phys. Rev. Lett. **96**, 013901 (2006); S. Randall, A. Brodsky, L. Burgess, and R. Green, in *Review of Progress in Quantitative Nondestructive Evaluation* (Plenum, New York, 2003), Vol. 22; M. Hamad, A. Brodsky, and L. Burgess, Appl. Spectrosc. **54**, 1506 (2000); M. Hamad, S. Kailasam, A. Brodsky, R. Han, J. Higgins, D. Thomas, R. Reed, and L. Burgess, *ibid.* **59**, 16 (2005), and references therein.
[13] Control of nanoparticle characteristics is important for a number of new optoelectronic technologies, in particular for quantum information devices where such particles are used as single photon emitters. See Z. Yuan, B. Kardynal, R. Stevenson, A. Shields, C. Lobo, K. Cooper, N. Beattie, D. Ritchie, and M. Pepper, Science **295**, 102 (2002).
[14] In the last few years, imaging techniques based on coherence loss in backscattering measurements have demonstrated considerable potential for qualitative *in vitro* study of biological tissues and blood. See V. Tuckin, X. Xu, and R. Wang, Appl. Opt. **41**, 258 (2002); A. Fercher, W. Dzeocler, C. Hitzenberger, and T. Lasser, Rep. Prog. Phys. **66**, 239 (2003).
[15] A. Brodsky and L. Burgess, Int. J. Mod. Phys. B **12**, 337 (2003).
[16] A. Kim and A. Ishimaru, J. Comput. Phys. **152**, 264 (1999), and references therein. The effect of Mie resonances in multiple scattering was recently considered by N. Ghosh, A. Pradhan, P. K. Gupta, S. Gupta, V. Jaiswal, and R. P. Singh, Phys. Rev. E **70**, 066607 (2004); see also G. Schweiger and H. Korn, J. Opt. Soc. Am. B **23**, 212 (2006). Among the different attempts to solve the radiative transfer problem for multiple scattering of classical waves, we mention the diagramic approach with partial diagram summation, the random matrix method [5] and the steady-state Langevin approach in B. Spivak and A. Zyuzin, Solid State Commun. **65**, 311 (1988). The fact that most of the approximations used for solutions to the considered problems have unknown validity limits makes their practical application problematic. The most advanced is the theory of wave propagation in the case of one-dimensional randomness, since the corresponding Green functions have a relatively simple exponential structure and it is possible to rely directly on the Fokker-Planck equation [24].
[17] See the description of Fermi pseudopotentials in G. Breit, Phys. Rev. **71**, 215 (1947); M. Goldberger and K. Watson, *Collision Theory* (Wiley, New York, 1964).
[18] R. Newton, *Scattering Theory of Waves and Particles* (Springer-Verlag, New York, 1982).
[19] The Fock's method is described in the book by W. Bogolubov and D. Shirkov, *Introduction to the Theory of Quantized Fields* (Wiley, New York, 1997) where it is applied for the solution of the Block-Nordsiek model in quantum field theory.
[20] A. Slavnov, Theor. Math. Phys. **22**, 177 (1975) (in Russian); G. Samelsohn and R. Mazar, Phys. Rev. E **54**, 5697 (1996).
[21] H. C. van de Hulst, *Light Scattering by Small Particles* (Wiley, New York, 1957); G. H. Meeten, Opt. Commun. **134**, 233 (1997).
[22] J. Bush, P. G. Davis, and M. Marcus, in *Fiber Optic Sensor Technology II, Proceedings of SPIE, Boston, 2000*, edited by B. Culshaw, J. A. Harrington, M. A. Marcus, and M. Saad (SPIE, Bellingham, WA, 2001), p. 71.
[23] 3000 Series Nanosphere Size Standards, 5000 Series Latex Microsphere Suspensions, Duke Scientific Corporation, Palo Alto, CA.
[24] I. Lifshitz, S. Gredescul, and L. Pasteur, *Introduction to the Theory of Disordered Systems* (Wiley, New York, 1988).
[25] When dynamic processes, including the Brownian diffusion of the particles near phase transition points, are important and ergodic theorem conditions are not fulfilled, it is necessary to take into account particular details of pair correlator time dependence. See F. Scheffold, S. E. Skipetrov, S. Romer, and P. Schurtenberger, Phys. Rev. E **63**, 061404 (2001).
[26] A. D. Mirlin, Phys. Rep. **326**, 259 (2000).
[27] The effects of finite coherence length on multiple scattering of light in random medium were emphasized by M. Tomita and H. Ikari, Phys. Rev. B **43**, 3716 (1991).
[28] S. Randall, A. Brodsky, and L. Burgess, Mod. Phys. Lett. B **19**, 181 (2005).
[29] A. Brodsky and A. Tsarevsky, J. Phys. A **20**, 3895 (1987).
[30] B. Berestetsky, E. Lifshitz, and L. Pitaevsky, *Quantum Electrodynamics*, 2nd ed. (Pergamon Press, Oxford, 1982).
[31] A. Agre and L. Rappoport, JETP **82**, 647 (1996).
[32] R. Sapienza, S. Mujumdar, C. Cheung, A. G. Yodh, and D. Wiersma, Phys. Rev. Lett. **92**, 033903 (2004).
[33] For a recent discussion of light propagation in optically active random media see M. Xu and R. R. Alfano, Phys. Rev. Lett. **95**, 213901 (2005); M. Matsuo, S. Miyoshi, M. Azuma, Y. Nakano, and Y. Bin, Phys. Rev. E **72**, 041403 (2005).
[34] P. C. Das and A. Puri, Phys. Rev. B **65**, 155416 (2002); A. Torricelli, A. Pifferi, L. Spinelli, R. Cubeddu, F. Martelli, S. Del Bianco, and G. Zaccanti, Phys. Rev. Lett. **95**, 078101 (2005).

[35] L. Cao, B. Nabet, and J. E. Spanier, Phys. Rev. Lett. **96**, 157402 (2006).
[36] G. Walrafen, J. Chem. Phys. **40**, 3249 (1964); H. Büning-Pfaue, Food Chem. Toxicol. **82**, 107 (2003).
[37] J. Israelachvili and H. Wennerstrom, Nature (London) **379**, 219 (1996); D. Marx, Science **303**, 634 (2004); A. Brodsky and W. Reinhardt, J. Phys. A **28**, 3453 (1995); B. Garrett, Science **303**, 1146 (2004); V. Ostroverkhov, G. A. Waychunas, and Y. R. Shen, Phys. Rev. Lett. **94**, 046102 (2005).